

1 **Separating balanced and unbalanced flow at the surface**
2 **of the Agulhas region using Lagrangian filtering**

3 **C. Spencer Jones^{1,2}, Qiyu Xiao³, Ryan P. Abernathey² and K. Shafer Smith³**

4 ¹Texas A&M University, College Station, TX

5 ²Columbia University, New York, NY

6 ³New York University, New York, NY

7 **Key Points:**

- 8 • Lagrangian filtering is used to separate balanced and unbalanced flow at the ocean
- 9 surface
- 10 • Removing super-inertial energy using Lagrangian filtering preserves some super-
- 11 inertial energy in the Eulerian frame
- 12 • Preserved surface velocities are associated with convergent fronts, suggesting that
- 13 they are balanced

Corresponding author: C Spencer Jones, spencerjones@tamu.edu

Abstract

The Surface Water and Ocean Topography (SWOT) satellite will measure altimetry on scales down to about 15km: at these scales, the sea-surface-height signature of inertia-gravity waves, including barotropic tides and internal tides, will be visible. However, inertia-gravity waves have little impact on tracer transport. This paper explores how to remove the portion of the surface velocity and sea surface height that is associated with inertia-gravity waves in the Agulhas region of a high-resolution ocean model (LLC4320). Various filtering methods are compared. Lagrangian filtering, a method that accounts for Doppler shifting of high-frequency motions by the low-frequency velocity field, is found to preserve flow that appears super-inertial in the reference frame of the Earth. Other methods do not preserve these motions as effectively. We show that the signal that is preserved by Lagrangian filtering is primarily associated with convergent fronts, suggesting that it is part of the balanced flow that has been Doppler shifted into the super-inertial range. Lagrangian filtering also removes some signal that appears sub-inertial in the reference frame of the Earth, but is really super-inertial motion that has been Doppler shifted into the sub-inertial range.

Plain Language Summary

Scientists often want to divide up the velocity at the surface into two parts: the part of the velocity that transports ocean tracers (like heat, salt and carbon), and the part of the velocity that is irrelevant for ocean tracer transport. Lagrangian filtering is a recently discovered method for doing this: it accounts for how the ocean velocities change the frequency of some of the signals we measure through Doppler shift. In this paper, we compare Lagrangian filtering to alternative methods and show that Lagrangian filtering seems to do a better job of revealing the part of the ocean surface velocity that transports tracers.

1 Introduction

Near-surface ocean currents are a critical component of the Earth system, mediating the transfer of heat, momentum, and trace gasses between ocean and atmosphere (Cronin et al., 2019; Elipot & Wenegrat, 2021). These currents regulate marine ecosystems by transporting nutrients and phytoplankton laterally within the eutrophic zone (Barton et al., 2010; Resplandy et al., 2011) and transporting marine debris and plastic pollution around the globe (Van Sebille et al., 2020). Observed ocean surface currents are also used to evaluate the accuracy and biases of numerical ocean models. As a result, the oceanographic community requires accurate and detailed knowledge of the state of ocean surface currents.

Satellite-based observations of sea-surface height (SSH), which is directly proportional to surface pressure, can be used to infer the velocities via geostrophic balance. Modern ocean altimetry products like Archiving, Validation, and Interpretation of Satellite Oceanographic data (AVISO) (Ducet et al., 2000) typically have grid resolution of around 0.25° and an effective resolution of approximately 200 km. At this scale, geostrophic balance holds well, and altimetry-derived near-surface geostrophic velocities are used in many studies of ocean currents (e.g., Niiler et al., 2003; Abernathey & Marshall, 2013; Mkhinini et al., 2014, and many others). Direct observations from drogued drifters, such as those from the NOAA Global Drifter Program, are an additional source of surface velocity data. While highly accurate, such measurements are relatively sparse, with approximately one drifter in every $5^\circ \times 5^\circ$ box of the ocean (Elipot et al., 2016).

The upcoming Surface Water and Ocean Topography (SWOT) satellite will measure altimetry at scales down to ~ 15 km (Morrow et al., 2019). These measurements have the potential to greatly enhance our understanding of ocean surface currents, particu-

63 larly at smaller scales. However, the SWOT measurements will also pose two distinct
 64 challenges for the estimation of velocities. First, the SWOT signal will presumably con-
 65 tain inertia-gravity waves (including barotropic and internal tides), which have an im-
 66 print on both the SSH and the velocity field (Zaron & Rocha, 2018). Second, even if the
 67 waves were to be removed somehow, geostrophy becomes increasingly inaccurate at SWOT
 68 scales, where the Rossby number approaches one.

69 In order to make progress on this problem, it is helpful to separate the internal tidal
 70 signal, as well as other non-tidal IGW components from the total SWOT SSH signal: this
 71 is a major focus of the SWOT science team research (Ponte et al., 2017; Lahaye et al.,
 72 2019; Klein et al., 2019). Some applications of near-surface velocities, particularly for
 73 the study of transport phenomena, benefit from a wave-free velocity field. The waves,
 74 while important and scientifically interesting for many reasons, make a minimal contri-
 75 bution to transport due to their quasi-linearity (Plumb, 1979; Balwada et al., 2018). Quasi-
 76 linear waves may displace tracer contours but don’t cause them to break; nonlinear in-
 77 teractions are usually required to create small-scale tracer structures that enable mix-
 78 ing in the vertical. The barotropic tidal signal is already removed from conventional al-
 79 timetric SSH as part of the data processing (Stammer et al., 2014).

80 Once the IGW signal has been removed from both the surface velocities and the
 81 SSH, the remaining SSH field is unlikely to be in simple geostrophic balance with the
 82 velocity field. Since SWOT will resolve smaller scales than previous altimeters, it will
 83 observe energetic eddies and fronts in which the Rossby number approaches one. Higher-
 84 order balances such as gradient-wind and semi-geostrophy may be more appropriate to
 85 describe flows at this scale: we call these motions “balanced ageostrophic” motions. Both
 86 balanced geostrophic and balanced ageostrophic motions are likely to be important for
 87 transporting tracers in the horizontal, but because geostrophic motion is approximately
 88 non-divergent, balanced ageostrophic motions are probably the most important flows for
 89 transporting tracers from the surface across the base of the mixed layer (Ferrari, 2011;
 90 Lévy et al., 2018; Mahadevan et al., 2020; Uchida et al., 2020). Hence it is important
 91 not to accidentally remove balanced ageostrophic motions when removing IGWs from
 92 the SWOT SSH signal.

93 The combined challenges of filtering waves and retaining balanced ageostrophic mo-
 94 tions mean that exploiting SWOT for inferring near-surface currents is far from trivial.
 95 Removing the IGW signal and studying the relationship between SSH and the balanced
 96 velocity field is a promising direction for future research. As a step towards estimating
 97 the balanced (transport-relevant) surface currents from SWOT data post launch, this
 98 paper investigates part 1 of the problem: how to accurately remove the IGW signal from
 99 near-surface ocean currents and preserve the transport-relevant part of the flow. We use
 100 a global eddy- and IGW-resolving GCM simulation, the MITgcm LLC4320. This sim-
 101 ulation provides a realistic truth signal with much of the same complexity as the real ocean,
 102 including both IGWs and balanced ageostrophic motions.

103 Using this model, we compare and evaluate three different filtering methods for re-
 104 moving IGWs and retaining the transport-relevant part of the surface velocity field. Each
 105 of these three methods has been used to remove or isolate IGWs in previous work, but
 106 the novelty of this paper is that we perform a detailed comparison of these methods at
 107 the ocean surface. The first method applies a frequency-based filter at a fixed location,
 108 the second method applies a frequency-based filter along particle pathways and the third
 109 method applies a frequency-wavenumber filter to a chosen region of the ocean. Below,
 110 we provide some background about each of these methods.

111 It has long been known that most inertia-gravity waves and internal waves have
 112 frequencies higher than the inertial frequency. One popular way of estimating the amount
 113 of energy in IGWs is to use a purely frequency-based method to isolate these motions.
 114 Furuichi et al. (2008); Richman et al. (2012) and Mazloff et al. (2020) all take a time-

115 series at each fixed physical location and apply a high-pass filter that preserves frequen-
 116 cies higher than the inertial frequency, before integrating over all frequencies to estimate
 117 the total energy in IGWs. A purely frequency-based method is also sometimes used to
 118 remove IGWs from the total velocity field. For example, Qiu et al. (2020) use a low-pass
 119 filter at each physical location to remove waves from their vertical velocity field. The first
 120 filtering method that we evaluate in this paper is purely frequency-based. Using this method,
 121 motions are measured at a fixed location on the Earth, with motions at frequencies lower
 122 than the inertial frequency labelled as balanced, and motions at frequencies higher than
 123 the inertial frequency labelled as wave-like.

124 Pinkel (2008) and Shakespeare and Hogg (2017) show that both balanced flows and
 125 IGWs are Doppler shifted by the large scale flow field. This means that fixed-location
 126 frequency filtering may be inaccurate, particularly in regions with fast background flows.
 127 Shakespeare and Hogg (2017) developed a method of filtering that accounts for this ef-
 128 fect. Lagrangian particles are seeded in the horizontal flow field and record the veloc-
 129 ity along their trajectories, i.e. in a flow-following coordinate system. Temporal (frequency)
 130 filtering is applied to the velocities recorded by each particle, after which the velocities
 131 are interpolated onto a regular grid. The second filtering method we use in this paper
 132 is Lagrangian filtering, based on the updated method by Shakespeare et al. (2021). In
 133 this method, motions are measured in flow-following coordinates, with motions at fre-
 134 quencies lower than the inertial frequency labelled as balanced and motions at frequen-
 135 cies higher than the inertial frequency are labelled as wave-like.

136 Torres et al. (2018) argue that instead of using a purely frequency-based method
 137 for identifying internal gravity waves, wavenumber information should also be used. Us-
 138 ing LLC4320 output for the Kurushio-Extension region, they plot the kinetic energy in
 139 frequency-wavenumber space. They find that the energy at frequencies higher than the
 140 tenth baroclinic mode tends to fall along discrete beams aligned with the dispersion re-
 141 lation of each of the baroclinic modes. In their figures, the energy at frequencies below
 142 this curve tends to be continuously spread in frequency wavenumber space, suggesting
 143 that it is associated with balanced motions. They subsequently estimate the amount of
 144 internal gravity wave energy in the model by integrating the energy at frequencies above
 145 the tenth baroclinic mode. The third filtering method in this paper labels motions with
 146 frequencies lower than the tenth baroclinic mode in frequency-wavenumber space as bal-
 147 anced, and motions with frequencies higher than the tenth baroclinic mode as wave-like.

148 This paper compares these three filtering methods: fixed-location frequency filter-
 149 ing (here called ω -filtering), Lagrangian filtering, and filtering frequencies higher than
 150 the tenth baroclinic mode (here called ω - k filtering). Our goal is to understand the dif-
 151 ferences between the three methods. We focus on Lagrangian filtering, which has not been
 152 substantially tested at the ocean surface. Our results suggest that in high-energy regions,
 153 Lagrangian filtering preserves a significant amount of horizontal flow that appears to be
 154 at super-inertial frequencies when measured at a fixed location. ω -filtering does not pre-
 155 serve these motions, and ω - k filtering only preserves some of these motions. We then ex-
 156 amine the velocities that are preserved by Lagrangian filtering, to evaluate whether their
 157 properties are consistent with balanced flow.

158 In addition to studying velocities, this paper examines how the three filtering meth-
 159 ods affect sea surface height. Both balanced and wave motions have an impact on local
 160 sea surface height, so any filter that is applied to the surface velocity field may also be
 161 useful for separating balanced and wave flow signatures in the sea surface height field.
 162 In particular, horizontal velocities that appear super-inertial but are preserved by La-
 163 grangian filtering are likely to be associated with sea surface height movement that ap-
 164 pears super-inertial but is also preserved by Lagrangian filtering.

165 Section 2 describes the region of LLC4320 used in this paper, together with the var-
 166 ious methods used to filter the velocity and SSH fields: section 2.1 describes the removal

167 of barotropic signals from the SSH and section 2.2 describes the different filtering meth-
 168 ods used in this work. In section 3.1, we plot the frequency spectrum of horizontal ve-
 169 locity and SSH for the three filtering methods. Section 3.2 describes the frequency-wavenumber
 170 spectra of horizontal velocity for the three filtering methods. Section 3.3 and section 3.4
 171 examine the properties of the velocities that are labeled as balanced by each filtering method,
 172 using joint probability density functions and the divergence combined with the fronto-
 173 genesis function. A summary of our results and some conclusions are presented in sec-
 174 tion 4.

175 2 Methods

176 This study focuses on 75 days of SSH and velocity data taken from the Agulhas
 177 region of the LLC4320 simulation (Rocha et al., 2016), which is a $1/48^\circ$ global config-
 178 uration of the MITgcm. The model includes tides, permits submesoscale variability and
 179 is able to resolve part of the IGW field (Savage et al., 2017). The large data volume of
 180 the LLC4320 model, together with the large computational cost of the Lagrangian fil-
 181 tering method, compelled us to focus on a limited region of the ocean. This region was
 182 selected because of the presence of strong mesoscale flow features, including the Agul-
 183 has retroflection and the Antarctic Circumpolar Current. The chosen region, which is
 184 the same region used in Sinha et al. (2019), is shown in figure 1, and the time period ex-
 185 tends from October to December 2011.

186 We compare several methods of partitioning the surface velocities, as detailed in
 187 section 2.2. One of these methods requires the data to be transformed into frequency-
 188 wavenumber space. Because of the curvature of the globe and the presence of land in the
 189 domain, it is not possible to apply this transformation to the whole domain at once. Hence,
 190 we choose to compare filtering methods in two regions of the domain: region A (shown
 191 by the blue box in figure 1) and region B (shown by the green box in figure 1). Region
 192 A is chosen to be a fairly typical region of the domain, whereas region B is chosen to be
 193 a highly energetic region with strong velocities across all space and time scales. Com-
 194 paring these regions allows us to evaluate the differences between filtering methods in
 195 a typical region and in a high-energy region.

196 2.1 Removing the barotropic signal from the sea surface height

197 The SSH contains variability that is associated with both balanced motions and
 198 with IGWs. However, it also contains a large amount of variability that is caused by mass
 199 changes in the water column, including the effects of barotropic tides, surface pressure
 200 changes and wind forcing. Because these barotropic motions have both subinertial and
 201 superinertial frequencies, the filtering methods described in section 2.2 are not designed
 202 to remove barotropic variability. Hence, we need to remove the barotropic part of the
 203 SSH variability before applying any other filtering method to the SSH field.

204 The tidal forcing of LLC4320 contains eight short-period tidal components, K_1 , O_1 ,
 205 P_1 , Q_1 , M_2 , S_2 , N_2 , and K_2 (Zhao et al., 2019), but LLC4320 has much more energy
 206 in the semidiurnal band than observations (Savage et al., 2017; Yu et al., 2019; Luecke
 207 et al., 2020). This is probably caused by the horizontal resolution, which resolves tidal
 208 forcing and propagation, but does not resolve the associated dissipative processes (Buijsman
 209 et al., 2020). Because of this difference from observations, an off-the-shelf tidal model
 210 tuned to the real ocean (e.g. the TPXO model, Egbert et al. (1994); Egbert and Ero-
 211 feeva (2002)) is unlikely to be suitable for removing the barotropic tide from sea surface
 212 height in LLC4320.

Another common way to filter out the barotropic signal (including barotropic tides,
 pressure- and wind-forced barotropic variability) is to use the steric height. The total

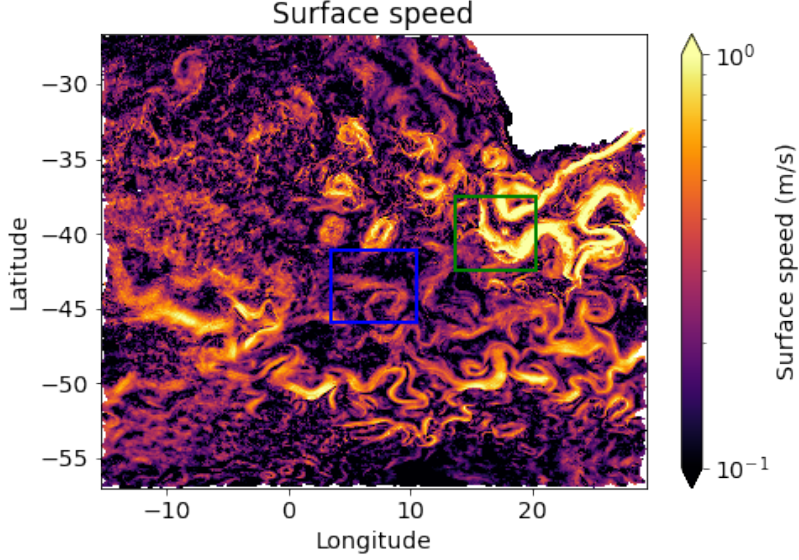


Figure 1. Snapshot of surface speed in our domain. The blue box is region A and the green box is region B. The white area in the north west of the domain is the southern part of Africa. The white areas around the edge indicate locations where seeded particles leave the domain within the 72 hour particle run.

SSH, η , is

$$\eta(x, y, t) = \underbrace{\frac{p'_b(x, y, t)}{\rho_0 g} - \frac{p_a(x, y, t)}{\rho_0 g}}_{\text{non-steric}} - \underbrace{\int_{-H}^0 \frac{\rho'(x, y, z, t)}{\rho_0} dz}_{\text{steric}}, \quad (1)$$

213 from Wang et al. (2018), where H is the ocean depth, $p'_b = p_b - \rho_0 g H$ represents the
 214 bottom pressure anomaly, p_a is the atmospheric pressure, and the density $\rho = \rho_0 + \rho'(x, y, z, t)$.
 215 The steric component of SSH is controlled by baroclinic motions, including balanced flows,
 216 internal waves and internal tides. The non-steric component is governed by the total wa-
 217 ter mass in the column, which is itself controlled by barotropic motions including the barotropic
 218 tide.

Following Wang et al. (2018), we rearrange equation (1) to calculate the steric height from the total SSH, the atmospheric pressure and the bottom pressure:

$$\eta_{\text{steric}} = \eta - \frac{p'_b}{\rho_0 g} + \frac{p_a}{\rho_0 g} \quad (2)$$

219 The power spectrum of the steric height is shown by the orange dashed line in figure 2.
 220 In both region A and region B, the tidal peaks are much less prominent in the steric SSH
 221 than in the raw SSH (compare blue and orange lines in figure 2). The steric height still
 222 retains a peak at M_2 and S_2 frequencies, because the semidiurnal tide forces IGW mo-
 223 tions at these frequencies.

224 If bottom pressure were not available, we could not calculate the steric height in
 225 this way. Because barotropic motions tend to have large spatial scales, we found that
 226 smoothing the SSH with a spatial filter (Grooms et al., 2021) that has a scale of 300km
 227 provides a good approximation of the steric height. The spectrum of the smoothed SSH
 228 is shown by the red dashed line in figure 2.

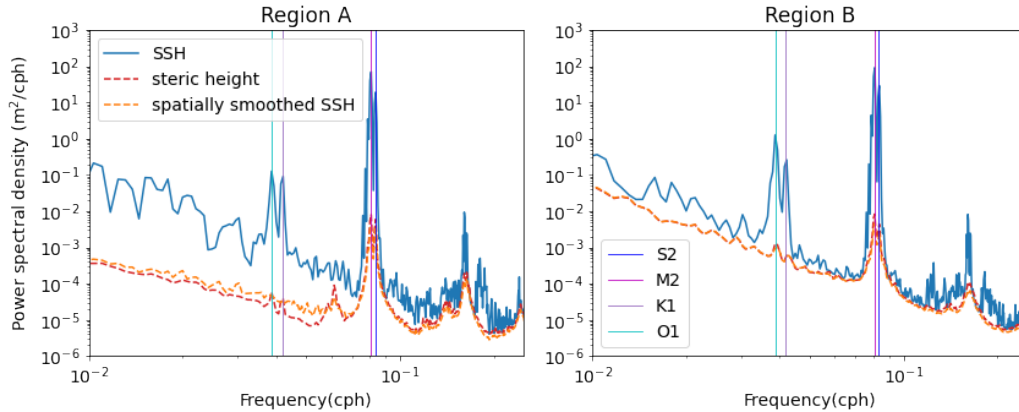


Figure 2. Power spectral density of the raw SSH (blue line), the steric height (orange dashed line) and the SSH smoothed with a spatial filter (red dashed line) in region A (left) and region B (right). Note that in region B the red dashed line is mostly obscured by the orange dashed line. Vertical lines mark the four highest-energy tidal frequencies, O_1 , K_1 , M_2 , S_2 .

229 Throughout the rest of this paper, whenever SSH is mentioned, the steric SSH is
 230 used.

2.2 Partitioning the balanced part and the IGW part of the flow

2.2.1 ω filtering

233 One popular way of partitioning balanced and unbalanced flows is to apply a fre-
 234 quency filter to timeseries collected at fixed physical locations (Furuichi et al., 2008; Rich-
 235 man et al., 2012; Mazloff et al., 2020). Motions with frequencies lower than the inertial
 236 frequency are labelled as balanced and motions with frequencies higher than the iner-
 237 tial frequency are labelled as waves. This method has the advantage of being very straight-
 238 forward and computationally cheap, and is used as a baseline in this paper.

In our version of frequency filtering, we apply a convolution filter to the timeseries
 of velocity and steric SSH at each point in x, y, z . We choose to use a sinc function as
 the window function for this filter, because its fourier transform is a tophat (see e.g. Lilly
 and Lettvin (2004)), so the field after ω -filtering, ϕ_ω is given by

$$\phi_\omega(t) = \int_{t-t_w}^{t+t_w} \phi(t) \operatorname{sinc}\left(\frac{f(t-\tau)}{1.1\pi}\right) d\tau, \quad (3)$$

239 where ϕ is the unfiltered field and $t_w = 36$ hours. The width of the sinc function is cho-
 240 sen to be $f/1.1$, where f is the local Coriolis parameter. This width is chosen so that
 241 near-inertial waves, which have frequencies close to f , will be removed by the filter, in
 242 addition to other IGWs with frequencies above f . Although the Fourier transform of a
 243 sinc function is a top-hat, ω -filtering does not completely remove all of the energies at
 244 frequencies higher than the inertial frequency because the sinc function is only applied
 245 over a 72-hour window: it is a good but imperfect low-pass filter.

2.2.2 Lagrangian filtering

247 As described above, Lagrangian filtering is a method where the filter is applied to
 248 a timeseries collected at a location that moves with the horizontal flow field. Lagrangian
 249 filtering requires computing Lagrangian trajectories from the Eulerian velocity field. We

250 accomplish this by using the MITgcm FLT package, together with offline mode, to com-
 251 pute particle trajectories from the velocity fields stored on disk (see Code Repository for
 252 numerical details of the configuration.) At time t_0 , particles are seeded at every grid point.
 253 Each particle is run forwards in time from time t_0 for 36 hours, and u, v , and η_{steric} are
 254 recorded along the trajectory of the particle. Each particle is also run backwards in time
 255 from time t_0 for 36 hours, and u, v , and η_{steric} are recorded along the trajectory of the
 256 particle. The forward and backward trajectories are concatenated to form a single 72 hour
 257 long trajectory, for which the midpoint is the position of the particle at time t_0 . This
 258 method was designed by Shakespeare et al. (2021) to prevent the particles from cluster-
 259 ing around regions of convergence, which would bias the spatial sampling of the parti-
 260 cles.

We choose to use the same filter window for Lagrangian filtering as for ω -filtering. For ω -filtering, the weighted moving average is taken over the timeseries at one location (i.e. the average moves in time only). For Lagrangian filtering, the weighted average is taken for each 72-hour trajectory, with a new 72-hour trajectory generated every timestep, and then the weighted averages are concatenated in time, so the field after Lagrangian filtering, ϕ_{lf} is given by

$$\phi_{lf}(t) = \int_{-t_w}^{t_w} \phi_l(t, \tau) \operatorname{sinc}\left(\frac{f\tau}{1.1\pi}\right) d\tau, \quad (4)$$

261 where $\phi_l(t_{init}, t_{traj})$ is the property field measured along particle trajectories initiated at
 262 time t_{init} and t_{traj} is the time the property was recorded relative to the time t_{init} .

263 Just as for ω -filtering above, the width of the filter is chosen to be $f/1.1$, where f
 264 is the local Coriolis parameter for the position of the particle at time t_0 .

265 **2.2.3 ω - k filtering**

266 Torres et al. (2018) propose a method of partitioning the balanced flow and the wave
 267 flow along a contour in frequency-wavenumber space. This contour is the dispersion curve
 268 of the tenth baroclinic mode: motions with frequencies above this contour are catego-
 269 rized as waves, and motions with frequencies below this contour are categorized as bal-
 270 anced flow. In this paper, we refer to this method as ω - k filtering.

271 To perform ω - k filtering, we first project the field $\phi(x, y, t)$ in regions A and B onto
 272 a tangent plane. We then apply a Tukey window and Fourier-transform the field $\phi(x, y, t)$
 273 to get $\phi(k_x, k_y, \omega)$. Frequencies higher than the tenth baroclinic mode are set to zero,
 274 and an inverse-Fourier transform is applied to the result. We then divide by the Tukey
 275 window to compensate for the reduction in energy associated with windowing. Because
 276 the Tukey window goes to zero at the beginning and end of the timeseries, and along the
 277 edges of the domain, in these regions, the results of ω - k filtering are very noisy. We chose
 278 to use a Tukey window because it has a large flat region across the center of the domain,
 279 in which windowing does not generate noise.

280 Because of the need to project onto a tangent plane, and the necessity of window-
 281 ing, ω - k filtering is not well-suited for estimating the balanced flow over a large region
 282 of physical space. It is more suitable for application to small regions. Torres et al. (2018)
 283 use ω - k filtering to calculate the balanced and wave energy in frequency-wavenumber space
 284 for small regions of physical space, without attempting to inverse-transform back to phys-
 285 ical space.

3 Results

3.1 Frequency spectrum

The power spectra described here were calculated from a two-week-long dataset of the filtered and unfiltered fields at hourly resolution. The power spectrum of the horizontal velocity in all three methods is shown in the top two panels of figure 3¹. In region A, the unfiltered horizontal velocity field (the orange line in figure 3a) has a spectral peak that spans the inertial frequency (shown by the vertical black line in figure 3) and the semidiurnal frequency (shown by the vertical blue line in figure 3), as well as additional peaks at various higher frequencies that are associated with overtides (Ray, 2007). Overall, there is more energy at high frequencies in region B than in region A. In region B, the spectrum of the unfiltered horizontal velocity has a small peak at the semidiurnal frequency, but is generally very smooth (orange line in figure 3b). The spectrum of unfiltered steric SSH is also smoother in region B than in region A (compare the orange lines in figure 3c and figure 3d). This suggests that a larger fraction of the total energy in region A is forced by tides and a smaller fraction of energy in region B is forced by tides. This does not necessarily imply that the tidally forced flow contains more energy in region A than in region B: it is also possible that region B contains more energy in non-tidally forced motions.

In region A, all three filtering methods reduce the high frequency energy of the horizontal velocity field, but ω -filtering removes the most energy from these frequencies (red dashed line in figure 3a and c). Even though the energy of the ω -filtered spectrum is much smaller than the energy of the unfiltered spectrum, the tidal peaks are preserved in the ω -filtered spectrum, because ω -filtering simply reduces the total energy at frequencies higher than f in the Eulerian frame.

Although they use exactly the same window function in their filter, there is a significant difference between ω -filtering and Lagrangian filtering. In fact at higher frequencies, Lagrangian filtering retains the most energy of all the filtering methods. In region A, the spectrum of the Lagrangian-filtered horizontal velocity is very smooth compared to the spectrum of the unfiltered flow (compare cyan and orange lines in figure 3a). The spectrum of the Lagrangian-filtered horizontal velocity has no peaks that are associated with overtides, and only a small peak at the inertial frequency. One interpretation of this result is that Lagrangian filtering is removing the energy in the horizontal velocity field at the tidal and overtidal frequencies. The spectrum of Lagrangian filtered SSH is also much smoother than the unfiltered spectrum, though some peaks are still visible (cyan dashed line in figure 3c and d). This suggests that Lagrangian filtering is mostly removing the energy in the SSH field at the tidal and overtidal frequencies. Another possibility is that the transformation to the Lagrangian frame blurs the tidal peaks, spreading their energy over a broad range of frequencies (Caspar-Cohen et al., 2022).

In region A, the spectrum of the ω - k filtered flow is also relatively smooth, except at frequencies higher than 4×10^{-1} cph (purple dashed line in figure 3a). This suggests that ω - k filtering is removing energy that is generated by tides. The ω - k -filtered spectrum has a much larger inertial peak, because the filter only removes frequencies higher than the 10th baroclinic mode, so it removes no frequencies lower than f . The roll-off of the ω -filter and Lagrangian filter are specifically designed to remove the inertial peak, because we do not expect near-inertial waves to contribute to tracer transport.

¹ We also computed rotary spectra, which reveal the difference between clockwise and counter-clockwise rotating flows, highlighting inertial oscillations. In these plots, for simplicity of presentation, we choose to focus just on the full spectrum, which is the sum of the clockwise and counter-clockwise components of the rotary spectrum.

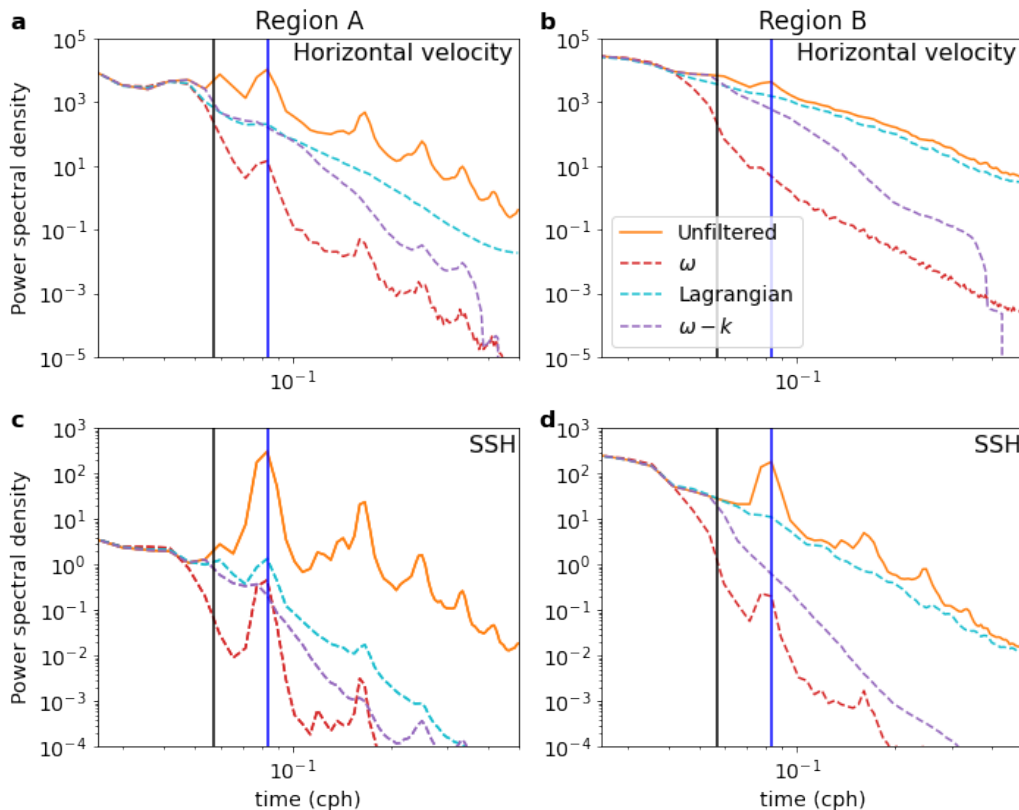


Figure 3. a) Power spectrum of horizontal velocity field calculated from the flow in region A, and b) power spectrum of horizontal velocity field calculated from the flow in region B. c) Power spectrum of SSH field calculated from the flow in region A and d) power spectrum of horizontal velocity field calculated from the flow in region B. In each panel, the orange solid line is the spectrum of the unfiltered field, the red dashed line is the spectrum of the ω -filtered field, the cyan dashed line is the spectrum of the Lagrangian filtered field and the purple dashed line is the spectrum of the $\omega-k$ filtered field. The vertical black line is the inertial frequency and the vertical blue line is the semidiurnal frequency.

331 In region B, tidal peaks above the semidiurnal frequency are not visible in the un-
 332 filtered spectrum of the horizontal velocity (orange line in figure 3a). The tidal peaks
 333 in the unfiltered SSH spectrum are smaller in region B than in region A (compare or-
 334 ange line in figure 3c and figure 3d). ω -filtering removes a large amount of energy from
 335 the horizontal velocity and SSH field, particularly at high frequencies (red dashed line
 336 in figure 3b and d). $\omega-k$ filtering removes less energy than ω -filtering, but it still reduces
 337 the energy at high frequencies by more than an order of magnitude (purple dashed line
 338 in figure 3b). Lagrangian filtering does not remove very much energy from the unfiltered
 339 horizontal velocity field, but it removes the small peak at the semidiurnal frequency (cyan
 340 line in figure 3b). Lagrangian filtering also removes the tidal peaks in the unfiltered SSH
 341 spectrum in region B (cyan line in figure 3d). One potential explanation is that Lagrangian
 342 filtering is mostly removing the energy in the SSH field at the tidal and overtidal frequen-
 343 cies in region B, but that most of the energy in region B is balanced.

344

3.2 Frequency-wavenumber spectra

345

346

347

348

349

350

351

352

353

The frequency spectrum summarizes a lot of information about the flow, but to better understand the characteristics of each of the filtering methods, it is helpful to calculate the power spectrum in frequency-wavenumber space. Figure 4 shows the isotropic frequency-wavenumber diagram for the surface velocity in region A and figure 5 shows the same analysis for region B. The unfiltered velocities (figures 4a and 5a) contain much more energy in region B. In region A, the energy at frequencies higher than the 10th baroclinic mode (shown by the green contour) is concentrated at the tidal harmonics, which suggests that this energy is associated with IGWs. In region B, the energy at frequencies higher than the 10th baroclinic mode is much smoother.

354

355

356

357

358

359

It is important to remember that these frequency-wavenumber diagrams are a representation of the amount of energy at each frequency and wavenumber measured in Eulerian space (regardless of what kind of filtering is applied). The authors are not aware of a method for calculating a frequency-wavenumber diagram in Lagrangian space, so the Lagrangian-filtered velocities are operated on in Eulerian space to create this diagram.

360

361

362

363

364

365

366

367

As expected, ω -filtering removes most of the energy at frequencies higher than the inertial frequency (figures 4b and 5b). However, Lagrangian filtering preserves a lot of energy with frequencies higher than the inertial frequency in the Eulerian frame. Lagrangian filtering is designed to remove energy at frequencies above the inertial frequency in a coordinate following the flow. Hence, energy that remains after Lagrangian filtering must be at subinertial frequencies in the Lagrangian frame, and must be Doppler-shifted into the superinertial range by velocities that change on longer timescales. In region A, the energy that is preserved by Lagrangian filtering generally has large wavenumbers.

368

369

370

371

372

373

374

The figures 4e and 5e show the difference between the frequency-wavenumber spectrum with Lagrangian filtering and the frequency-wavenumber spectrum with ω -filtering. In both regions, the Lagrangian-filtered velocities have more energy at superinertial frequencies in the Eulerian frame and less energy at subinertial frequencies in the Eulerian frame. This indicates that Doppler shifting is likely happening in both directions: ω -filtering spuriously removes flow that is Doppler shifted into the superinertial range, and spuriously retains flow that is Doppler shifted into the subinertial range.

375

376

377

378

379

380

381

382

The frequency-wavenumber diagram after ω - k filtering is shown in the figures 4d and 5d for comparison with Lagrangian filtering. Because there is less energy above the green curve in region A than region B, ω - k filtering removes a larger amount of superinertial energy in region B. Much more of the low- to intermediate-wavenumber superinertial energy in region B is retained by Lagrangian filtering, suggesting that much of this energy is associated with balanced flow that has been Doppler-shifted into the superinertial range. Region B is characterized by stronger currents, so more pronounced Doppler shift is expected.

383

3.3 Vorticity-strain JPDFs

Another way to estimate the separation of wave velocity and balanced velocity is by considering the joint probability density function (JPDF) of the normalized-by- f surface vorticity ζ/f , strain $\sigma/|f|$, and divergence δ/f , where

$$\zeta = v_x - u_y \quad (5)$$

$$\sigma = \sqrt{(u_x - v_y)^2 + (v_x + u_y)^2} \quad (6)$$

$$\delta = u_x + v_y. \quad (7)$$

384

385

Balwada et al. (2021) found that the vorticity-strain JPDFs of submesoscale-rich flows are characterized by a clear frontal signature, appearing as concentrations along the ± 1

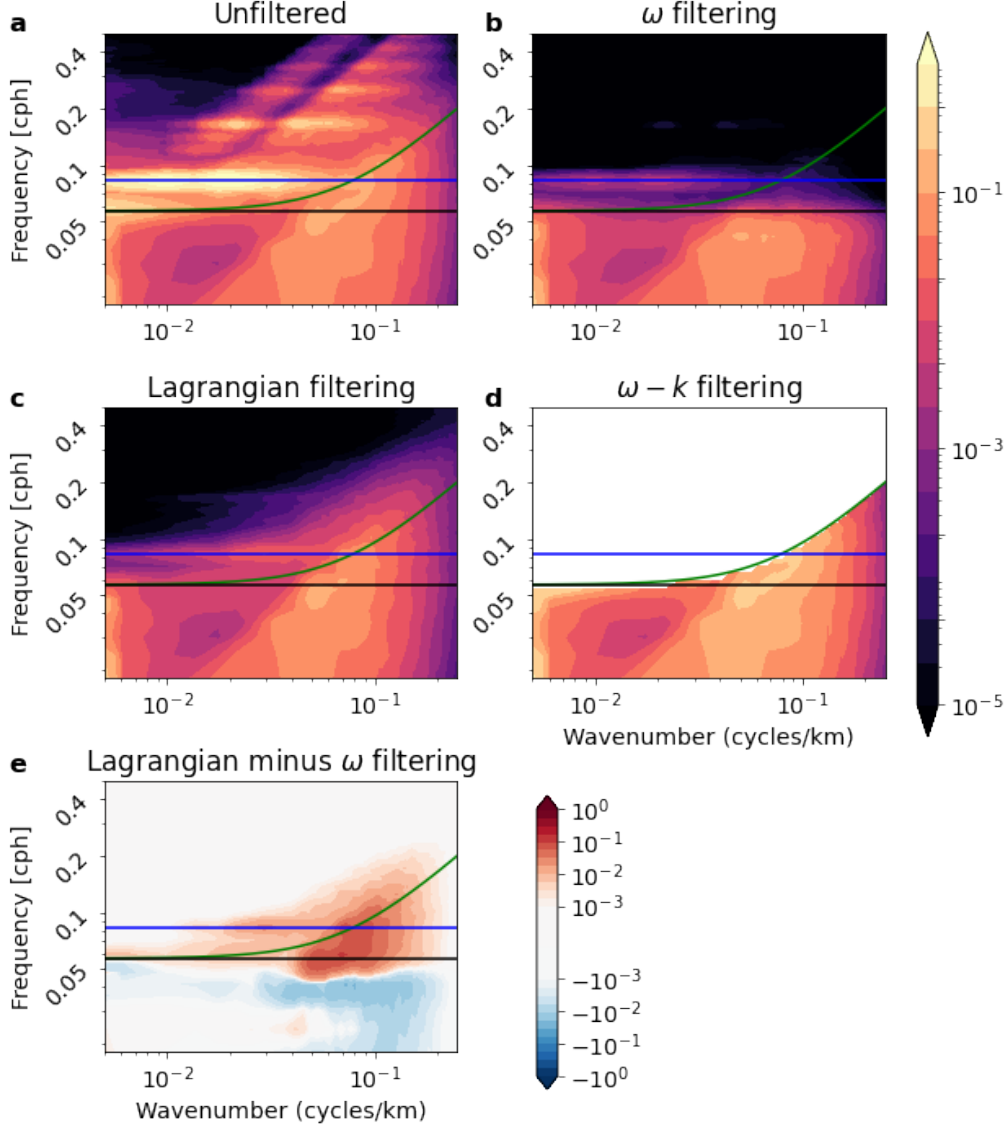


Figure 4. The isotropic frequency-wavenumber spectrum of horizontal velocity field calculated from the flow inside region A, the blue box of figure 1, for a) the unfiltered velocity field, b) the ω -filtered velocity, c) the Lagrangian filtered velocity and d) the ω - k filtered velocity. e) The frequency-wavenumber spectrum of Lagrangian filtered horizontal velocity minus the frequency-wavenumber spectrum of the ω -filtered velocity. The black horizontal line is the inertial frequency and the blue horizontal line is the semidiurnal frequency. The green line is the tenth baroclinic mode. The isotropic frequency-wavenumber spectrum is obtained by azimuthally-averaging over all values of k , where $k = \sqrt{k_x^2 + k_y^2}$.

386 slope lines, because $|\zeta| \approx \sigma$ for fronts. Moreover, because large frontal vertical veloci-
 387 ties generate vortex stretching in the vorticity equation, submesoscale fronts are highly
 388 asymmetric and skewed toward positive vorticity, which appears as a long tail on the cy-
 389 clonic side of the JPDF. By contrast, wave-dominated super-inertial flows tend to have $|\zeta| \ll$
 390 $|\delta| \sim \sigma$, and thus have vorticity-strain JPDFs that are mostly symmetric and centered

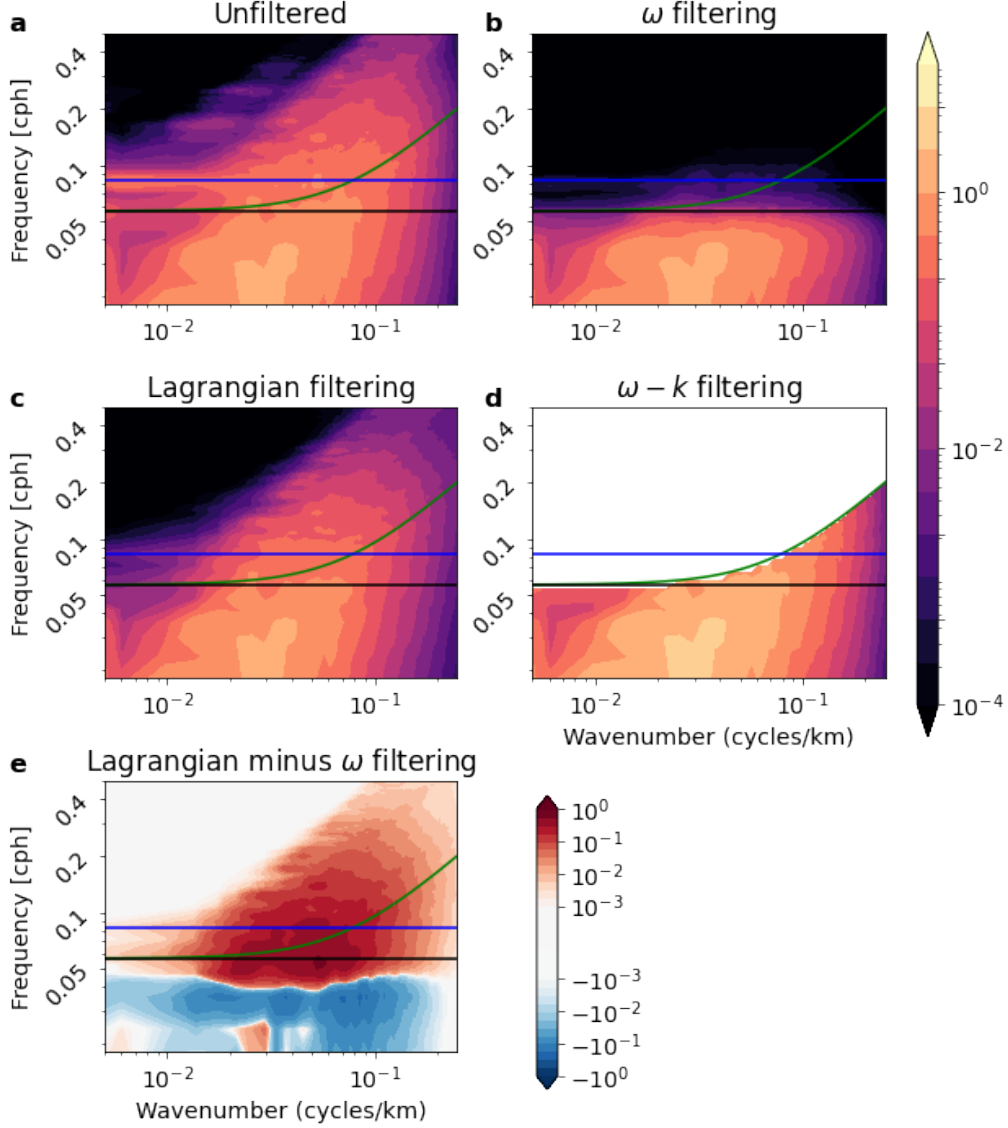


Figure 5. The isotropic frequency-wavenumber spectrum of horizontal velocity field calculated from the flow inside region B, the green box of figure 1, for a) the unfiltered velocity field, b) the ω -filtered velocity, c) the Lagrangian filtered velocity and d) the ω - k filtered velocity. e) The frequency-wavenumber spectrum of Lagrangian filtered horizontal velocity minus the frequency-wavenumber spectrum of the ω -filtered velocity. The black horizontal line is the inertial frequency and the blue horizontal line is the semidiurnal frequency. The green line is the tenth baroclinic mode. The isotropic frequency-wavenumber spectrum is obtained by azimuthally-averaging over all values of k , where $k = \sqrt{k_x^2 + k_y^2}$.

391

around the origin². Thus by considering the vorticity-strain JPDFs calculated from the

² Consider, for example, a shallow water inertia-gravity wave, which has $\zeta = f|\mathbf{k}|/\omega \cos \theta$ and $\delta = |\mathbf{k}| \sin \theta$, where \mathbf{k} is the horizontal wavenumber and $\theta = \mathbf{k} \cdot \mathbf{x} - \omega t$. Thus $\zeta/\delta \sim f/\omega$, so that for high-frequency waves, $|\zeta| \ll |\delta|$. Moreover, $\sigma = \sqrt{\zeta^2 + \delta^2}$, so for high-frequency waves, $\sigma \sim |\delta|$.

392 filtered and unfiltered velocity fields, we can get a sense of how well the various filter-
393 ing methods preserve frontal features and remove waves.

394 Figure 6 shows, for regions A and B, the vorticity-strain JPDFs of the unfiltered
395 velocity, the ω -filtered velocity, the Lagrangian-filtered velocity, and the unfiltered-minus-
396 filtered velocity fields for each filtering method (specifically, we compute the JPDFs of
397 the velocity field obtained by subtracting the filtered from the unfiltered velocity). The
398 JPDF of the unfiltered velocity is more asymmetric and extends much farther along the
399 $\zeta = \sigma$ line in region B than in region A, consistent with the former being character-
400 ized by higher energy and more submesoscale fronts (compare the panels in the top row
401 of figure 6). The JPDFs of the unfiltered velocity fields for each region share roughly the
402 same shapes with their filtered velocity fields, using any filtering method, indicating that
403 both the filtered and unfiltered velocity fields contain some balanced flows associated with
404 fronts.

405 The JPDFs of the unfiltered-minus-filtered velocities (i.e. the velocities categorized
406 as waves) are different between filtering methods. In region A, the JPDFs are relatively
407 symmetric, indicating that a few submesoscale fronts are mis-categorized as wave-like.
408 However, in region B, the JPDF of the unfiltered-minus-filtered flow are asymmetric for
409 ω -filtering and ω - k filtering, but symmetric with Lagrangian-filtering. This suggests that,
410 at least in region B, where balanced ageostrophic flows are strong, ω -filtering and ω - k
411 filtering spuriously filters out parts of balanced flow (mis-categorizing them as wave-like),
412 while Lagrangian filtering does not. Moreover, in both regions, ω -filtering removes larger
413 vorticity and strain values, while Lagrangian-filtering preserves them. These JPDFs pro-
414 vide additional evidence that in both regions, Lagrangian filtering is more effective at
415 removing waves, while preserving balanced ageostrophic flows, than ω -filtering.

416 3.4 Divergence in physical space

The horizontal velocities associated with waves are more divergent than the hor-
zontal velocities associated with geostrophically-balanced flows (see e.g. Bühler et al.
(2014)). However, upper-ocean submesoscale flows are characterized by strongly conver-
gent fronts. An important test of filtering methods is the degree to which they retain
the divergence associated with submesoscale fronts while removing the divergence as-
sociated with wave-like flows. We show the divergence of the surface velocity field for
a representative time snapshot in figure 7 (region A) and in figure 8 (region B). We also
plot the frontogenesis function,

$$F_s = \mathbf{Q}_s \cdot \nabla_h b, \quad (8)$$

417 where $\mathbf{Q}_s = -\left(\frac{\partial u}{\partial x} \frac{\partial b}{\partial x} + \frac{\partial v}{\partial x} \frac{\partial b}{\partial y} + \frac{\partial w}{\partial x} \frac{\partial b}{\partial z}, \frac{\partial u}{\partial y} \frac{\partial b}{\partial x} + \frac{\partial v}{\partial y} \frac{\partial b}{\partial y} + \frac{\partial w}{\partial y} \frac{\partial b}{\partial z}\right)$. Large positive values
418 indicate that the flow field is acting to increase the buoyancy gradient (Hoskins, 1982;
419 Capet et al., 2008; Brannigan et al., 2015). Hence, these large values tend to be present
420 at fronts.

421 Figures 7 and 8 show that ω -filtering, Lagrangian filtering and ω - k filtering all re-
422 duce the divergence of the velocity field significantly. In region A, ω -filtering and Lagrangian
423 filtering reduce the divergence more than ω - k filtering (compare figure 7b, c, and d with
424 figure 7a), even in regions with a low frontogenesis function. This suggests that ω - k fil-
425 tering does not remove all the waves. Both ω -filtering and Lagrangian filtering preserve
426 higher divergences in the region where the frontogenesis function is large and positive
427 (the region surrounded by a thin black contour).

428 In region B, ω -filtering reduces the divergence the most out of all the filtering meth-
429 ods (Figure 8b). Lagrangian filtering preserves much more negative divergences in the
430 region where the frontogenesis function is large and positive (Figure 8c). This suggests
431 that in region B, Lagrangian filtering preserves more of the ageostrophically-balanced
432 flow associated with convergent fronts.

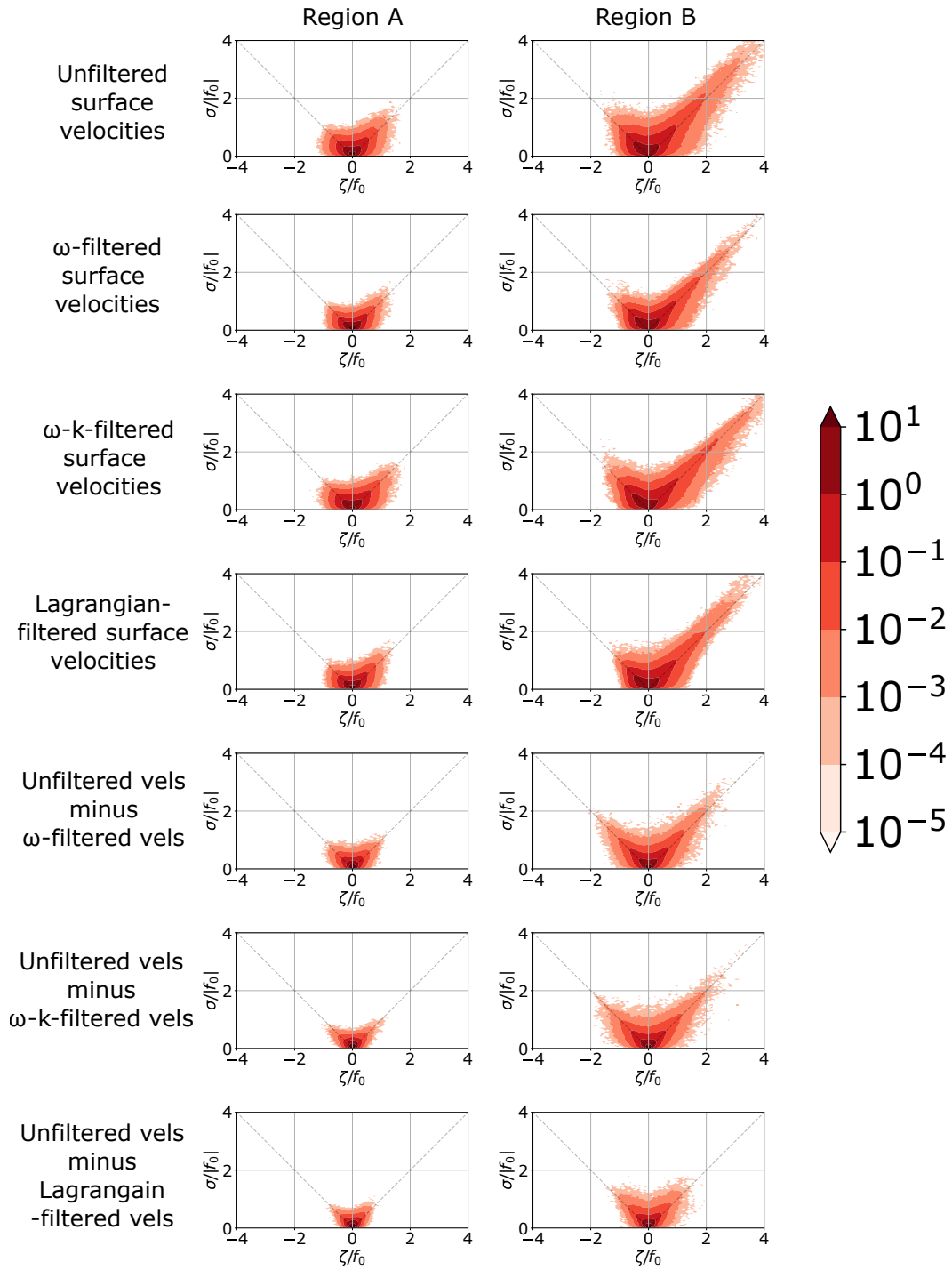


Figure 6. Vorticity-strain joint probability density functions calculated from surface velocities in region A (left) and in region B (right). The dashed lines are the $|\zeta| = \sigma$ lines: submesoscale fronts tend to be concentrated just above the cyclonic $\zeta = \sigma$ line (Balwada et al., 2021). For the ω - k filtered velocities are projected onto a tangent plane before the JPDF is calculated, but all other JPDFs are calculated without projection (projection onto a tangent plane introduces a small error in the vorticity and strain fields).

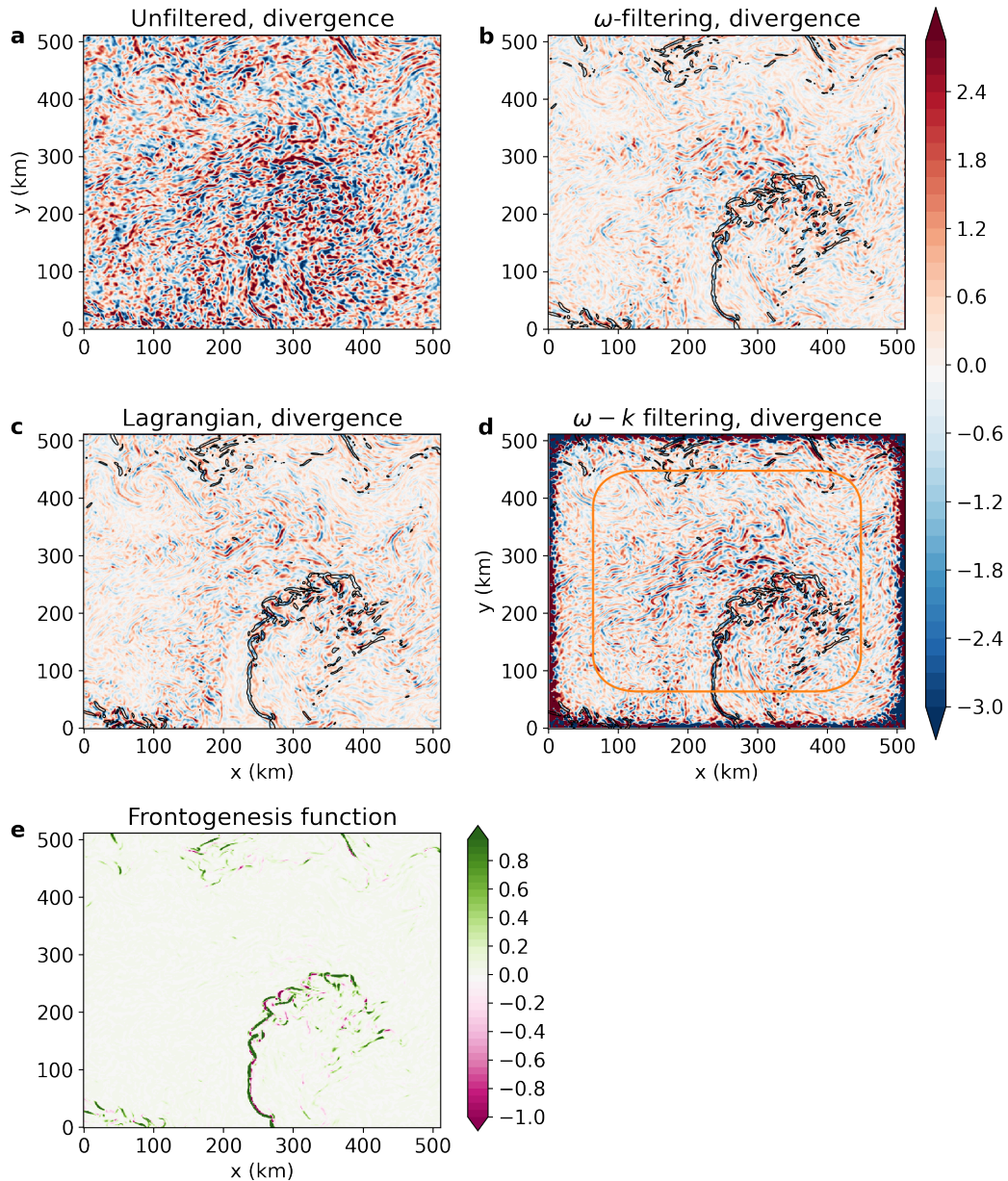


Figure 7. a-d) Divergence ($\times 10^5 \text{s}^{-1}$) of unfiltered and filtered velocities on day 35 in region A, the blue box of figure 1, and e) the frontogenesis function ($\times 10^{14} \text{kg}^2/\text{m}^8/\text{s}$). Thin black contours show the 0.2 contour of the frontogenesis function. Inside the orange contour, the window function used in ω - k filtering is greater than 0.5: inside this contour, inaccuracies due to windowing should be negligible.

433

3.5 Geostrophy

Across most of the ocean, surface velocities that are estimated by applying geostrophy to the unfiltered sea-surface height field are not good predictors of the true sea-surface velocity field (Yu et al., 2021). Removing the inertia gravity wave signal removes velocities that are not in geostrophic balance, so we might expect that the filtered velocities

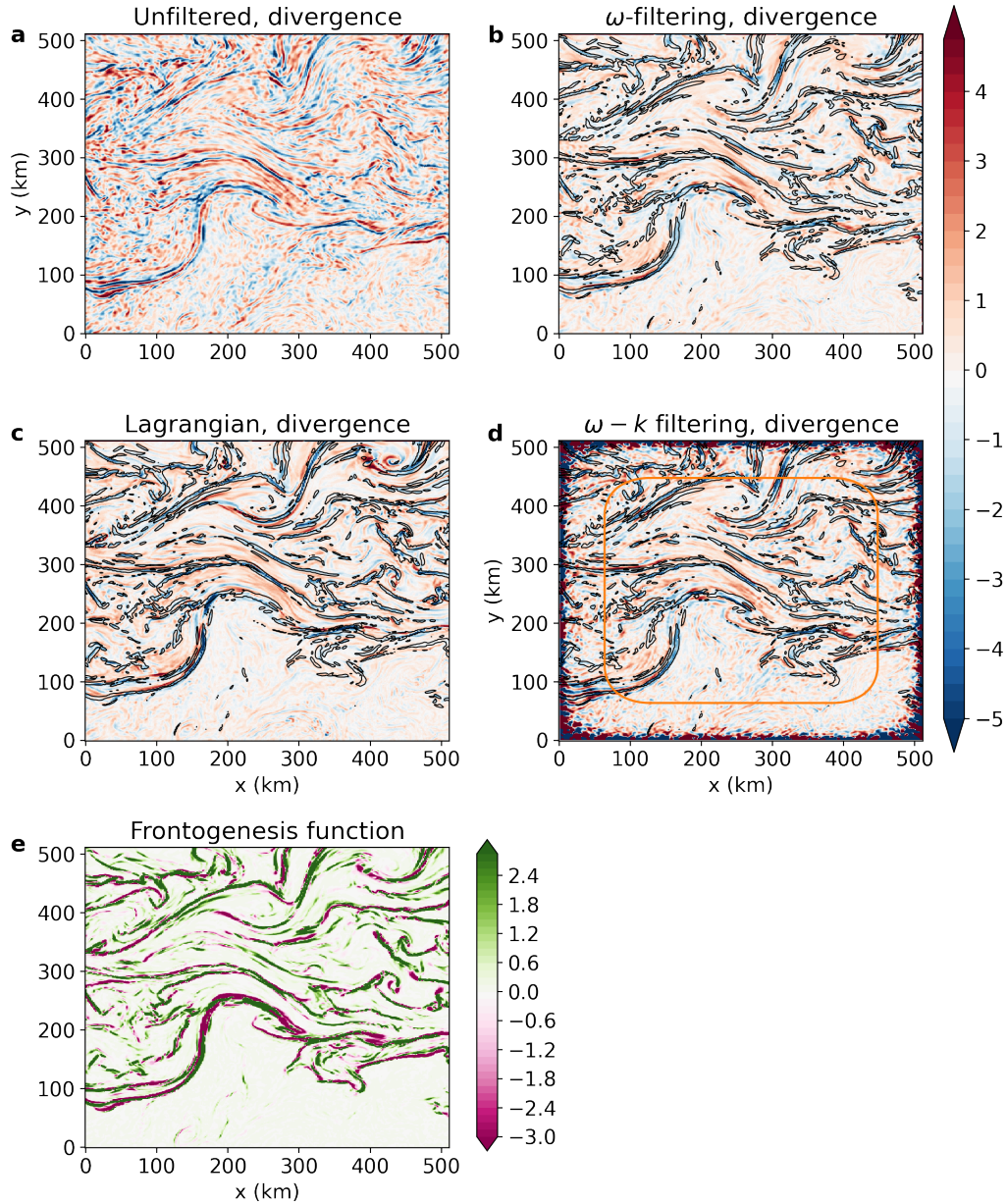


Figure 8. a-d) Divergence ($\times 10^5 \text{s}^{-1}$) of unfiltered and filtered velocities on day 35 inside the green box of figure 1, and e) the frontogenesis function ($\times 10^{14} \text{kg}^2/\text{m}^8/\text{s}$). Black contours show the 1 contour of the frontogenesis function. Inside the orange contour, the window function used in $\omega - k$ filtering is greater than 0.5: inside this contour, inaccuracies due to windowing should be negligible.

will be more geostrophic than the unfiltered velocities. In figure 9, we estimate the geostrophic velocity by naively applying the geostrophic equation to the sea-surface-height field, and then take the root-mean-square difference between the surface speed and this SSH-derived

geostrophic speed estimate:

$$\text{RMS}^{ij} = \frac{1}{A} \int \sqrt{\frac{\left(\frac{1}{T} \int (|\mathbf{v}^i| - |\mathbf{v}_{\text{ssh}}^j|)^2 dt\right)}{\sigma_t(|\mathbf{v}^i|)}} dA, \quad (9)$$

434 where \mathbf{v} is the velocity at the surface, i is the type of filtering used on the velocity field
 435 (no filtering, ω -filtering, Lagrangian filtering or ω - k filtering), \mathbf{v}_{ssh} is the SSH-derived
 436 velocity field, j is the type of filtering used on the SSH field, and T is the total length
 437 of the timeseries after filtering (70days). We normalize this root-mean-square difference
 438 by the pointwise standard deviation of the velocity field, $\sigma_t(|\mathbf{v}^i|)$.

439 In region A (left panel in figure 9), applying any kind of filtering to the velocity
 440 or sea surface height generates fields that obey geostrophic balance marginally more ac-
 441 curately than the unfiltered fields. All three filtered velocity fields are approximately equally
 442 similar to the raw-SSH-derived geostrophic velocity estimate (top row of the left panel
 443 of figure 9), indicating that no filter is better than any other at selecting for geostrophic
 444 flows. The raw-SSH-derived geostrophic velocity field is based on the unfiltered steric
 445 SSH, so it contains a significant amount of variability from waves. Applying a filter to
 446 the SSH before creating the SSH-derived geostrophic velocity estimates leads to more
 447 agreement between the velocity field and the SSH-derived velocity field (compare top row
 448 of the left panel of figure 9 with subsequent rows). This suggests that the SSH is strongly
 449 influenced by high frequency motions, which are not geostrophic. Even though Lagrangian
 450 filtering may preserve more of the balanced flow at high frequencies, Lagrangian filter-
 451 ing is no better than ω -filtering for picking out geostrophic balance in region A. Hence,
 452 the high frequency flow that is preserved by Lagrangian filtering is mostly not in geostrophic
 453 balance.

454 In region B, filtering the velocity field does not significantly improve its agreement
 455 with the raw-SSH-derived geostrophic velocity estimate (top row of right panel in fig-
 456 ure 9). This is probably because region B contains a lot of submesoscale activity and most
 457 of the balanced flows in region B are ageostrophic. Applying an ω -filter or ω - k filter to
 458 the SSH field leads to more agreement between SSH-derived velocity estimate and the
 459 surface velocities: both of these filters remove high frequency motions of all kinds from
 460 the SSH field. Applying a Lagrangian filter to the SSH is generally less effective at pick-
 461 ing out geostrophy, suggesting that a lot of the motion preserved by Lagrangian filter-
 462 ing in region B is not geostrophic (even if it is balanced).

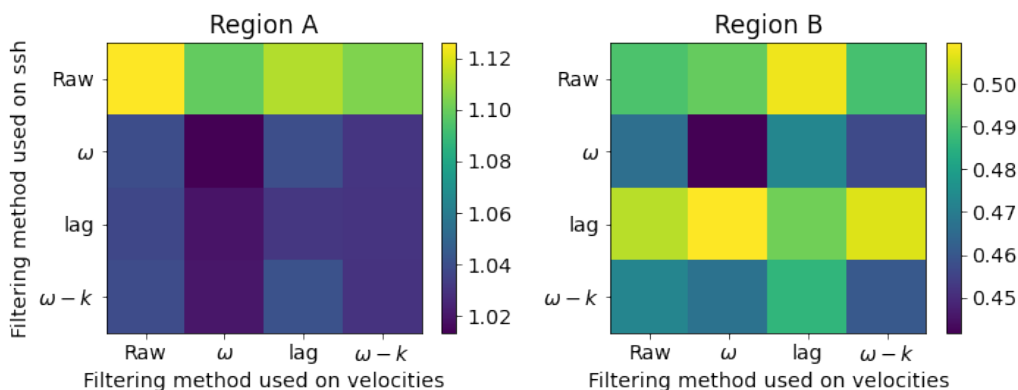


Figure 9. Normalized root mean square difference (RMS^{ij} in equation (9)) between the unfiltered surface speed and the surface speed calculated by applying the geostrophic equation to sea-surface height for the blue box of figure 1 (left) and the green box of figure 1 (right).

463 4 Conclusions

464 SWOT offers an unprecedented opportunity to observe the global sea surface height
 465 down to scales of $O(10\text{ km})$, an order of magnitude improvement over the current gen-
 466 eration of altimeters (Fu and Ferrari, 2008). While at coarser scales, geostrophic balance
 467 allows accurate estimation of upper-ocean velocity from SSH, no such simple balance can
 468 be used to extract velocities from SWOT measurements. The lack of a simple balance
 469 to relate SSH to velocities poses not only a challenge to determining the latter, it also
 470 implies that the velocity field itself is more complex at these scales. In particular, it will
 471 contain components due to both ageostrophic balances, as well as inertia-gravity wave
 472 signals. The latter do not impact tracer transport, but act as a noise that complicates
 473 studies of the relationship between the SSH and the transport-relevant velocity field.

474 Here we have investigated an approach to solving one part of the complex puzzle
 475 posed by SWOT data: filtering wave signals from high-resolution data. The methods con-
 476 sidered include simple low-pass filtering in frequency (termed ω -filtering), combined wavenumber-
 477 frequency filtering (ω - k filtering, after Torres et al. (2018)), and Lagrangian filtering (af-
 478 ter Shakespeare and Hogg (2017); Shakespeare et al. (2021)).

479 ω -filtering is computationally very cheap, and it removes all motions at frequen-
 480 cies higher than f in the Eulerian frame from the surface velocity field. However, this
 481 process removes some motions that have been Doppler shifted to higher frequencies, in-
 482 cluding some motions associated with fronts and filaments. ω - k filtering, which was pro-
 483 posed by Torres et al. (2018), was designed based on the frequency-wavenumber prop-
 484 erties of flow in the Kuroshio Extension region. Frequencies higher than the tenth baro-
 485 clinic mode were observed to fall in discrete bands, suggesting they were associated with
 486 IGWs. This paper shows that in region B (our high energy region), this is no longer true:
 487 much of the energy at frequencies higher than the tenth baroclinic mode appears smooth
 488 in the frequency-wavenumber diagram shown in figure 5. The use of the tenth baroclinic
 489 mode may work in the Kuroshio Extension region, but there is no guarantee that it is
 490 useful for partitioning the flow in much of the rest of the ocean. Although ω - k filtering
 491 is computationally cheaper than Lagrangian filtering, we do not think that it is broadly
 492 applicable across most regions of the ocean.

493 Lagrangian filtering preserves motions that appear superinertial in the reference
 494 frame of the Earth, but are subinertial in the reference frame of the flow. This is con-
 495 sistent with previous work by Callies et al. (2020), which showed that the velocity field
 496 observed at a fixed location in the North Atlantic is predominantly rotational even at
 497 apparently superinertial frequencies. Callies et al. (2020) hypothesized that they were
 498 observing balanced flow that was Doppler shifted into the superinertial range. In this pa-
 499 per we confirm that surface velocities in the superinertial range include Doppler-shifted
 500 motions, at least in the LLC4320 simulation.

501 In high-energy regions, Lagrangian filtering appears to be more to preserve flows
 502 close to filaments and fronts. It is likely that these flows are ageostrophically balanced.
 503 In realistic simulations (and in the ocean itself), there is not a clean metric to evaluate
 504 whether velocities are balanced, but we make use of the frontogenesis function and vorticity-
 505 strain JPDFs to understand the features of the velocities that are preserved by Lagrangian
 506 filtering. We show that it particularly preserves convergent flows in areas of frontoge-
 507 nesis. Preserving these convergent flows is likely to be important for modeling the ver-
 508 tical transport of ocean tracers. The differences between Lagrangian filtering and the
 509 other methods are larger in regions with high energy flows. More research is needed to
 510 identify when Lagrangian filtering is likely to be useful, and when it is an unnecessary
 511 computational expense.

512 Lagrangian filtering also removes motions that appear subinertial in the reference
 513 frame of the Earth, but are superinertial in the reference frame of the flow. This has not

514 been observed before but consistent with the effects of Doppler shift hypothesized by Pinkel
515 (2008). Because IGWs generally have lower energies than balanced motions, Doppler shifted
516 IGWs do not have much effect on the total energy measured in the subinertial range.

517 We do not expect that the methods described here will be directly applied to SWOT
518 observations. This paper represents the first step in the journey to extract the transport-
519 relevant velocity field from high-resolution SSH observations. Once we understand how
520 to isolate balanced motions from the full velocity and SSH fields, we hope to create a
521 large dataset that contains snapshots of filtered SSH, together with the filtered surface
522 velocity field associated with each SSH snapshot. This dataset will be used as a truth
523 signal from which to learn how to extract transport-relevant velocity field from low-temporal
524 resolution SSH snapshots. The method that is developed will then be applied to SWOT
525 observations, and will be used to estimate ocean surface velocities.

526 This multistep process is involved, but has the potential to produce surface veloc-
527 ity data with high value to the scientific community. Alongside this approach, we ad-
528 vocate the use of intermediate approaches like using vorticity-strain joint PDFs (Balwada
529 et al., 2021) to short-circuit directly to inference of transport-active flow from velocity,
530 even with waves in latter.

531 **Acknowledgments**

532 All authors acknowledge support from NASA award 80NSSC20K1142. This work would
533 not have been possible without the tools provided by and maintained by the Pangeo com-
534 munity (<https://pangeo.io/>). The code repository for this work is at [https://github](https://github.com/cspencerjones/separating-balanced)
535 [.com/cspencerjones/separating-balanced](https://github.com/cspencerjones/separating-balanced). The datasets used to create figures 3-7
536 are available at <https://doi.org/10.5281/zenodo.6561068>. Figures 1 and 2 can be
537 created from the LLC4320 data that is available via the pangeo catalog: [https://catalog](https://catalog.pangeo.io/browse/master/ocean/LLC4320/)
538 [.pangeo.io/browse/master/ocean/LLC4320/](https://catalog.pangeo.io/browse/master/ocean/LLC4320/).

539 **References**

- 540 Abernathey, R. P., & Marshall, J. (2013). Global surface eddy diffusivities derived
541 from satellite altimetry. *Journal of Geophysical Research: Oceans*, 118(2),
542 901–916.
- 543 Balwada, D., Smith, K. S., & Abernathey, R. (2018). Submesoscale vertical veloc-
544 ities enhance tracer subduction in an idealized antarctic circumpolar current.
545 *Geophysical Research Letters*, 45(18), 9790–9802.
- 546 Balwada, D., Xiao, Q., Smith, S., Abernathey, R., & Gray, A. R. (2021). Verti-
547 cal fluxes conditioned on vorticity and strain reveal submesoscale ventilation.
548 *Journal of Physical Oceanography*.
- 549 Barton, A. D., Dutkiewicz, S., Flierl, G., Bragg, J., & Follows, M. J. (2010). Pat-
550 terns of diversity in marine phytoplankton. *Science*, 327(5972), 1509–1511.
- 551 Brannigan, L., Marshall, D. P., Naveira-Garabato, A., & Nurser, A. G. (2015). The
552 seasonal cycle of submesoscale flows. *Ocean Modelling*, 92, 69–84.
- 553 Bühler, O., Callies, J., & Ferrari, R. (2014). Wave–vortex decomposition of one-
554 dimensional ship-track data. *Journal of Fluid Mechanics*, 756, 1007–1026.
- 555 Buijsman, M. C., Stephenson, G. R., Ansong, J. K., Arbic, B. K., Green, J. M.,
556 Richman, J. G., ... Zhao, Z. (2020). On the interplay between horizontal
557 resolution and wave drag and their effect on tidal baroclinic mode waves in
558 realistic global ocean simulations. *Ocean Modelling*, 152, 101656.
- 559 Callies, J., Barkan, R., & Garabato, A. N. (2020). Time scales of submesoscale flow
560 inferred from a mooring array. *Journal of Physical Oceanography*, 50(4), 1065–
561 1086.
- 562 Capet, X., McWilliams, J. C., Molemaker, M. J., & Shchepetkin, A. (2008).
563 Mesoscale to submesoscale transition in the california current system. part

- 564 ii: Frontal processes. *Journal of Physical Oceanography*, 38(1), 44–64.
- 565 Caspar-Cohen, Z., Ponte, A., Lahaye, N., Carton, X., Yu, X., & Le Gentil, S. (2022).
- 566 Characterization of internal tide incoherence: Eulerian versus lagrangian per-
- 567 spectives. *Journal of Physical Oceanography*.
- 568 Cronin, M. F., Gentemann, C. L., Edson, J., Ueki, I., Bourassa, M., Brown, S., ...
- 569 others (2019). Air-sea fluxes with a focus on heat and momentum. *Frontiers in*
- 570 *Marine Science*, 430.
- 571 Ducet, N., Le Traon, P.-Y., & Reverdin, G. (2000). Global high-resolution mapping
- 572 of ocean circulation from topex/poseidon and ers-1 and-2. *Journal of Geophys-*
- 573 *ical Research: Oceans*, 105(C8), 19477–19498.
- 574 Egbert, G. D., Bennett, A. F., & Foreman, M. G. (1994). Topex/poseidon tides esti-
- 575 mated using a global inverse model. *Journal of Geophysical Research: Oceans*,
- 576 99(C12), 24821–24852.
- 577 Egbert, G. D., & Erofeeva, S. Y. (2002). Efficient inverse modeling of barotropic
- 578 ocean tides. *Journal of Atmospheric and Oceanic technology*, 19(2), 183–204.
- 579 Elipot, S., Lumpkin, R., Perez, R. C., Lilly, J. M., Early, J. J., & Sykulski, A. M.
- 580 (2016). A global surface drifter data set at hourly resolution. *Journal of*
- 581 *Geophysical Research: Oceans*, 121(5), 2937–2966.
- 582 Elipot, S., & Wenegrat, J. (2021). Vertical structure of near-surface currents–
- 583 importance, state of knowledge, and measurement challenges.
- 584 Ferrari, R. (2011). A frontal challenge for climate models. *Science*, 332(6027), 316–
- 585 317.
- 586 Furuichi, N., Hibiya, T., & Niwa, Y. (2008). Model-predicted distribution of wind-
- 587 induced internal wave energy in the world’s oceans. *Journal of Geophysical Re-*
- 588 *search: Oceans*, 113(C9).
- 589 Grooms, I., Loose, N., Abernathy, R., Steinberg, J., Bachman, S. D., Marques, G.,
- 590 ... Yankovsky, E. (2021). Diffusion-based smoothers for spatial filtering of
- 591 gridded geophysical data. *Journal of Advances in Modeling Earth Systems*,
- 592 13(9), e2021MS002552.
- 593 Hoskins, B. J. (1982). The mathematical theory of frontogenesis. *Annual review of*
- 594 *fluid mechanics*, 14(1), 131–151.
- 595 Klein, P., Lapeyre, G., Siegelman, L., Qiu, B., Fu, L.-L., Torres, H., ... Le Gentil, S.
- 596 (2019). Ocean-scale interactions from space. *Earth and Space Science*, 6(5),
- 597 795–817.
- 598 Lahaye, N., Gula, J., & Rouillet, G. (2019). Sea surface signature of internal tides.
- 599 *Geophysical Research Letters*, 46(7), 3880–3890.
- 600 Lévy, M., Franks, P. J., & Smith, K. S. (2018). The role of submesoscale currents in
- 601 structuring marine ecosystems. *Nature communications*, 9(1), 1–16.
- 602 Lilly, J. M., & Lettvin, E. (2004). The “switch-on” problem for linear time-invariant
- 603 operators. *Signal processing*, 84(4), 763–784.
- 604 Luecke, C. A., Arbic, B. K., Richman, J. G., Shriver, J. F., Alford, M. H., Ansong,
- 605 J. K., ... others (2020). Statistical comparisons of temperature variance
- 606 and kinetic energy in global ocean models and observations: Results from
- 607 mesoscale to internal wave frequencies. *Journal of Geophysical Research:*
- 608 *Oceans*, 125(5), e2019JC015306.
- 609 Mahadevan, A., Pascual, A., Rudnick, D. L., Ruiz, S., Tintoré, J., & D’Asaro, E.
- 610 (2020). Coherent pathways for vertical transport from the surface ocean to
- 611 interior. *Bulletin of the American Meteorological Society*, 101(11), E1996–
- 612 E2004.
- 613 Mazloff, M. R., Cornuelle, B., Gille, S. T., & Wang, J. (2020). The importance of
- 614 remote forcing for regional modeling of internal waves. *Journal of Geophysical*
- 615 *Research: Oceans*, 125(2), e2019JC015623.
- 616 Mkhinini, N., Coimbra, A. L. S., Stegner, A., Arsouze, T., Taupier-Letage, I., &
- 617 Béranger, K. (2014). Long-lived mesoscale eddies in the eastern mediterranean
- 618 sea: Analysis of 20 years of aviso geostrophic velocities. *Journal of Geophysical*

- 619 *Research: Oceans*, 119(12), 8603–8626.
- 620 Morrow, R., Fu, L.-L., Arduin, F., Benkiran, M., Chapron, B., Cosme, E., . . . oth-
 621 ers (2019). Global observations of fine-scale ocean surface topography with
 622 the surface water and ocean topography (swot) mission. *Frontiers in Marine*
 623 *Science*, 6, 232.
- 624 Niiler, P., Maximenko, N., Panteleev, G., Yamagata, T., & Olson, D. (2003). Near-
 625 surface dynamical structure of the kuroshio extension. *Journal of Geophysical*
 626 *Research: Oceans*, 108(C6).
- 627 Pinkel, R. (2008). Advection, phase distortion, and the frequency spectrum of
 628 finescale fields in the sea. *Journal of physical oceanography*, 38(2), 291–313.
- 629 Plumb, R. (1979). Eddy fluxes of conserved quantities by small-amplitude waves.
 630 *Journal of atmospheric sciences*, 36(9), 1699–1704.
- 631 Ponte, A. L., Klein, P., Dunphy, M., & Le Gentil, S. (2017). Low-mode inter-
 632 nal tides and balanced dynamics disentanglement in altimetric observations:
 633 Synergy with surface density observations. *Journal of Geophysical Research:*
 634 *Oceans*, 122(3), 2143–2155.
- 635 Qiu, B., Chen, S., Klein, P., Torres, H., Wang, J., Fu, L.-L., & Menemenlis, D.
 636 (2020). Reconstructing upper-ocean vertical velocity field from sea surface
 637 height in the presence of unbalanced motion. *Journal of Physical Oceanogra-*
 638 *phy*, 50(1), 55–79.
- 639 Ray, R. D. (2007). Propagation of the overtide m4 through the deep atlantic ocean.
 640 *Geophysical research letters*, 34(21).
- 641 Resplandy, L., Lévy, M., Madec, G., Pous, S., Aumont, O., & Kumar, D. (2011).
 642 Contribution of mesoscale processes to nutrient budgets in the arabian sea.
 643 *Journal of Geophysical Research: Oceans*, 116(C11).
- 644 Richman, J. G., Arbic, B. K., Shriver, J. F., Metzger, E. J., & Wallcraft, A. J.
 645 (2012). Inferring dynamics from the wavenumber spectra of an eddying global
 646 ocean model with embedded tides. *Journal of Geophysical Research: Oceans*,
 647 117(C12).
- 648 Rocha, C. B., Gille, S. T., Chereskin, T. K., & Menemenlis, D. (2016). Seasonality
 649 of submesoscale dynamics in the kuroshio extension. *Geophysical Research Let-*
 650 *ters*, 43(21), 11–304.
- 651 Savage, A. C., Arbic, B. K., Alford, M. H., Ansong, J. K., Farrar, J. T., Menemenlis,
 652 D., . . . others (2017). Spectral decomposition of internal gravity wave sea
 653 surface height in global models. *Journal of Geophysical Research: Oceans*,
 654 122(10), 7803–7821.
- 655 Shakespeare, C. J., Gibson, A. H., Hogg, A. M., Bachman, S. D., Keating, S. R.,
 656 & Velzeboer, N. (2021). A new open source implementation of lagrangian
 657 filtering: A method to identify internal waves in high-resolution simulations.
 658 *Journal of Advances in Modeling Earth Systems*, 13(10), e2021MS002616.
- 659 Shakespeare, C. J., & Hogg, A. M. (2017). Spontaneous surface generation and inter-
 660 rior amplification of internal waves in a regional-scale ocean model. *Journal of*
 661 *Physical Oceanography*, 47(4), 811–826.
- 662 Sinha, A., Balwada, D., Tarshish, N., & Abernathey, R. (2019). Modulation of lat-
 663 eral transport by submesoscale flows and inertia-gravity waves. *Journal of Ad-*
 664 *vances in Modeling Earth Systems*, 11(4), 1039–1065.
- 665 Stammer, D., Ray, R., Andersen, O. B., Arbic, B., Bosch, W., Carrère, L., . . . others
 666 (2014). Accuracy assessment of global barotropic ocean tide models. *Reviews*
 667 *of Geophysics*, 52(3), 243–282.
- 668 Torres, H. S., Klein, P., Menemenlis, D., Qiu, B., Su, Z., Wang, J., . . . Fu, L.-L.
 669 (2018). Partitioning ocean motions into balanced motions and internal gravity
 670 waves: A modeling study in anticipation of future space missions. *Journal of*
 671 *Geophysical Research: Oceans*, 123(11), 8084–8105.
- 672 Uchida, T., Balwada, D., P Abernathey, R., A McKinley, G., K Smith, S., & Lévy,
 673 M. (2020). Vertical eddy iron fluxes support primary production in the open

- 674 southern ocean. *Nature communications*, *11*(1), 1–8.
- 675 Van Sebille, E., Aliani, S., Law, K. L., Maximenko, N., Alsina, J. M., Bagaev, A., ...
676 others (2020). The physical oceanography of the transport of floating marine
677 debris. *Environmental Research Letters*, *15*(2), 023003.
- 678 Wang, J., Fu, L.-L., Qiu, B., Menemenlis, D., Farrar, J. T., Chao, Y., ... Flexas,
679 M. M. (2018). An observing system simulation experiment for the calibration
680 and validation of the surface water ocean topography sea surface height
681 measurement using in situ platforms. *Journal of Atmospheric and Oceanic
682 Technology*, *35*(2), 281–297.
- 683 Yu, X., Ponte, A. L., Elipot, S., Menemenlis, D., Zaron, E. D., & Abernathey, R.
684 (2019). Surface kinetic energy distributions in the global oceans from a high-
685 resolution numerical model and surface drifter observations. *Geophysical
686 Research Letters*, *46*(16), 9757–9766.
- 687 Yu, X., Ponte, A. L., Lahaye, N., Caspar-Cohen, Z., & Menemenlis, D. (2021).
688 Geostrophy assessment and momentum balance of the global oceans in a tide-
689 and eddy-resolving model. *Journal of Geophysical Research: Oceans*, *126*(10),
690 e2021JC017422.
- 691 Zaron, E. D., & Rocha, C. B. (2018). Internal gravity waves and meso/submesoscale
692 currents in the ocean: anticipating high-resolution observations from the swot
693 swath altimeter mission. *Bulletin of the American Meteorological Society*,
694 *99*(9), ES155–ES157.
- 695 Zhao, Z., Wang, J., Menemenlis, D., Fu, L.-L., Chen, S., & Qiu, B. (2019). Decom-
696 position of the multimodal multidirectional m2 internal tide field. *Journal of
697 Atmospheric and Oceanic Technology*, *36*(6), 1157–1173.